

Cassiopeia A: dust factory revealed via submillimetre polarimetry

L. Dunne,^{1*} S. J. Maddox,¹ R. J. Ivison,^{2,3} L. Rudnick,⁴ T. A. DeLaney,⁵
B. C. Matthews,⁶ C. M. Crowe,¹ H. L. Gomez,⁷ S. A. Eales⁷ and S. Dye⁷

¹*School of Physics & Astronomy, University of Nottingham, University Park, Nottingham NG7 2RD*

²*UK Astronomy Technology Centre, Royal Observatory, Blackford Hill, Edinburgh EH9 3HJ*

³*Institute for Astronomy, University of Edinburgh, Blackford Hill, Edinburgh EH9 3HJ*

⁴*Department of Astronomy, University of Minnesota, 116 Church Street, SE Minneapolis, MN 55455, USA*

⁵*MIT Kavli Institute, 77 Massachusetts Avenue, Room NE80-6079, Cambridge, MA 02139, USA*

⁶*Herzberg Institute of Astrophysics, National Research Council of Canada, 5071 West Saanich Road, Victoria, BC, V9E 2E7, Canada*

⁷*Department of Physics & Astronomy, Cardiff University, Queen's Buildings, The Parade, Cardiff CF24 3AA*

Accepted 2008 December 22. Received 2008 December 4; in original form 2008 September 3

ABSTRACT

If Type II supernovae – the evolutionary end points of short-lived, massive stars – produce a significant quantity of dust ($>0.1 M_{\odot}$) then they can explain the rest-frame far-infrared emission seen in galaxies and quasars in the first Gyr of the Universe. Submillimetre (submm) observations of the Galactic supernova remnant, Cas A, provided the first observational evidence for the formation of significant quantities of dust in Type II supernovae. In this paper, we present new data which show that the submm emission from Cas A is polarized at a level significantly higher than that of its synchrotron emission. The orientation is consistent with that of the magnetic field in Cas A, implying that the polarized submm emission is associated with the remnant. No known mechanism would vary the synchrotron polarization in this way and so we attribute the excess polarized submm flux to cold dust within the remnant, providing fresh evidence that cosmic dust can form rapidly. This is supported by the presence of both polarized and unpolarized dust emission in the north of the remnant where there is no contamination from foreground molecular clouds. The inferred dust polarization fraction is unprecedented ($f_{\text{pol}} \sim 30$ per cent) which, coupled with the brief time-scale available for grain alignment (<300 yr), suggests that supernova dust differs from that seen in other Galactic sources (where $f_{\text{pol}} = 2\text{--}7$ per cent) or that a highly efficient grain alignment process must operate in the environment of a supernova remnant.

Key words: supernovae: individual: Cassiopeia A – dust, extinction – supernova remnants – submillimetre.

1 INTRODUCTION

The large quantities of dust seen in high-redshift quasars and galaxies (Priddey et al. 2003; Priddey, Ivison & Isaak 2008; Wang et al. 2007, 2008), at a time when the Universe was only ~ 1 Gyr old, suggest that a rapid mechanism for dust production must operate. Type II supernovae (SNe) are good candidates for these dust factories as they evolve to a dust-producing phase in only a few hundred Myr and contain a high abundance of heavy elements. Theory predicts that each Type II SNe should produce $\sim 0.1\text{--}1 M_{\odot}$ of dust (Todini & Ferrara 2001; Nozawa et al. 2003; Bianchi & Schneider 2007) and, if true, this can account for the dust observed at high redshift (Morgan & Edmunds 2003; Dwek, Galliano & Jones 2007).

Evidence for this quantity of dust forming in young SNe in the local Universe has been scant and controversial. Observations from

mid-/far-infrared (IR) satellites (*IRAS*, *ISO* and *Spitzer*) detect only warm dust and find orders of magnitude less than predicted by theory (Dwek et al. 1987; Lagage et al. 1996; Douvion et al. 2001; Borkowski et al. 2006; Sugerman et al. 2006; Williams, Chu & Gruendl 2006; Blair et al. 2007; Meikle et al. 2007), for example the maximum warm dust mass inferred for Cas A from *Spitzer* data is $0.03\text{--}0.05 M_{\odot}$ (Rho et al. 2008). Submillimetre (submm) observations of Cas A seemed to provide the first evidence for large ($\sim 2 M_{\odot}$) quantities of colder dust manufactured in the SN explosion (Dunne et al. 2003, hereafter D03). However, subsequent observations of CO and OH towards Cas A suggested that some or all of the submm emission may originate from dust in a foreground molecular cloud complex rather than the remnant (Krause et al. 2004; Wilson & Batrla 2005). Although the level of foreground contamination is highly uncertain – because of the difficulties in converting a molecular line intensity into a submm flux density – the molecular data have cast doubt on the idea that significant quantities of dust can form rapidly in SNe.

*E-mail: loretta.dunne@nottingham.ac.uk

Another explanation for the submm excess, this time without a significant mass of dusty material, was proposed by Dwek (2004). Elongated iron needles with a much higher submm emissivity than canonical dust can also account for the far-IR and submm spectral energy distribution (SED) of Cas A. If present in the general ISM, they should contaminate the polarization signal from the CMB which could have importance consequences (e.g. Bowden et al. 2004).

Polarimetry at 850 μm is extremely challenging but provides one way to test the competing hypotheses for the submm emission in Cas A: cold dust in Cas A, foreground contamination, or iron needles. We report such observations here, with the paper organized as follows: Section 2 describes the submm and radio polarimetry; Section 3 presents the results and investigates the robustness of the submm polarimetry; in Section 4, we use the polarimetry to place constraints on the fraction of submm emission arising from the remnant and comment on the implications for grain alignment theories.

2 OBSERVATIONS AND DATA REDUCTION

2.1 Submm observations

Our submm observations took place during 2004 October 17–18 using the Submillimetre Common-User Bolometer Array (SCUBA) polarimeter (Murray et al. 1997; Holland et al. 1999; Greaves et al. 2003) at the 15-m James Clerk Maxwell Telescope (JCMT), Hawaii.¹ We used SCUBA at 850 μm where the array contains 37 bolometers. The instrument comprises a rotating quartz half-wave plate and a fixed photo-lithographic-grid analyser in a module that is placed in front of the SCUBA cryostat’s entrance window. The weather conditions were exceptional – very stable with very little sky noise, with $\tau_{230\text{GHz}} \lesssim 0.04$ throughout. Two positions on the bright rim of Cas A were observed (Fig. 1), one in the west (hereafter W) and one in the north (hereafter N). Our original Cas A submm map (D03) was taken in SCUBA’s ‘scan-map’ mode; for the polarimetry we were forced to make a ‘jiggle’ map, stepping the secondary mirror of the telescope in a 16-point pattern in order to provide a fully sampled image at 850 μm , whilst chopping a distance of 180 arcsec at around 7 Hz (the maximum possible displacement) – to remove the atmospheric signal, and nodding the telescope every 32 s to correct for slowly varying sky gradients. The chop positions were chosen to avoid the remnant as much as possible; Fig. 1 shows the location of the fields and their chop positions. A detailed discussion of the potential effects of chopping on to emission in the reference positions is presented in Section 3. A full 16-point jiggle was taken at each of 16 positions of the half-wave plate, separated by 22:5. Thus 16 maps complete one full rotation, yielding four redundant polarization observations. We co-added five and three such observations for the western and northern regions, respectively, yielding total integration times of 65 min for the western region and 45 min for the northern region.

The submm data were reduced using the SCUBA User Reduction Facility (SURF; Jenness & Lightfoot 1998) and POLPACK (Berry & Gledhill 2001). The basic analysis consisted of removing the nod, flat-fielding, correcting for extinction, flagging bad bolometers, removing sky noise and clipping noisy data. For the extinction cor-

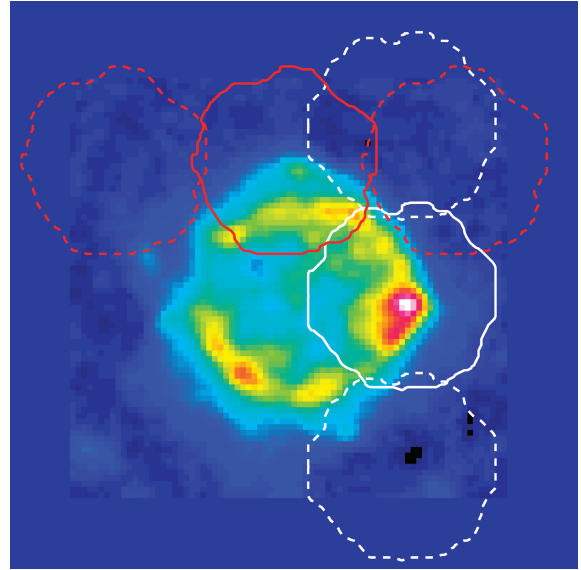


Figure 1. Cas A at 850 μm , from D03, showing the regions observed with the SCUBA polarimeter. On-source fields are denoted by solid lines while chop positions are shown by dashed lines. Position W (white) is the brightest region at radio and submm wavelengths and is coincident with a CO emission-line peak. Position N (red) is where the dust-to-synchrotron ratio is lowest and where there is no foreground emission.

rection, we employed a polynomial fit to the Caltech Submillimeter Observatory’s 230-GHz skydip data. To remove any residual time-varying sky level, we made preliminary maps in order to choose bolometers lying in emission-free regions and then subtracted their median signal in every second of integration from the full array. We experimented with different sky bolometers and different thresholds for removing noisy bolometers to assess their impact on the polarimetry measurements. We found some small changes in the derived polarization parameters but all maps were consistent within the errors (see Section 3 for more details).

Instrumental polarization (IP) arises through the SCUBA optics and the GORE-TEX membrane in front of the dish (Greaves et al. 2003). IP is elevation-dependent and can be characterized by making observations of unpolarized planets. The IP was removed using the SURF task REMIP, which uses a look-up table of bolometer IPs and corrects for the elevation at the time of the observation. The uncertainty in the IP removal is ± 0.5 per cent (Matthews, Wilson & Fiege 2001). Once treated in this way, each integration was re-gridded separately using a Gaussian weighting function with a scale of 7 arcsec (approximately half the full width at half-maximum (FWHM) for SCUBA at 850 μm) on to 6.2-arcsec pixels (the step size of the jiggle pattern), ready for the polarization analysis. From each complete polarimetry observation, four degenerate maps are made for each of the four equivalent wave-plate angles. The four maps at each angle are stacked and the variance for each pixel calculated from the scatter between the four maps. POLPACK was then used to derive the Stokes U , Q and I values for each pixel in each complete polarimetry observation by fitting the following function to the data (Sparks & Axon 1999)

$$I_k' = \frac{t}{2} [I + \epsilon(Q \cos 2\phi_k + U \sin 2\phi_k)],$$

where I_k' is the expected intensity in image k , ϕ_k is the position angle of the wave plate after correction for the parallactic angle for image k , t is the analyser transmission factor and ϵ is the polarizing

¹ The JCMT is operated by the Joint Astronomy Centre on behalf of the Science and Technology Facilities Council of the United Kingdom, the Netherlands Organization for Scientific Research and the National Research Council of Canada.

efficiency factor. The error in each Stokes parameter is derived from the input variances.

These I , Q and U images were then median stacked for repeat observations and a final data cube was created. Polarization fractions, p , and position angles (PAs), θ , were derived from the Stokes parameters (Hildebrand et al. 2000) after correcting for the Ricean bias - that is the increase in p that results from constraining p to be positive even when Q and U are consistent with $p = 0$. Ricean bias is a significant effect for low signal-to-noise measurements ($\text{SNR} \lesssim 2$).

We define the normalized Stokes parameters and associated errors as

$$u = U/I; \quad q = Q/I$$

$$\sigma_q = \left(\frac{\sigma_I^2 q^2 + \sigma_Q^2}{I^2} \right)^{1/2}; \quad \sigma_u = \left(\frac{\sigma_I^2 u^2 + \sigma_U^2}{I^2} \right)^{1/2}.$$

Debiased p values are calculated using

$$p = \frac{\sqrt{q^2 + u^2 - \Delta}}{I} \times 100 \text{ per cent}, \quad (1)$$

where the bias is given by

$$\Delta = \frac{q^2 \sigma_q^2 + u^2 \sigma_u^2}{q^2 + u^2}. \quad (2)$$

The error in p is $\sigma_p = \sqrt{\Delta} \times 100$ per cent. The polarization PA - the position of the electric field vector measured relative to Celestial North - is given by

$$\theta = 0.5 \arctan \left(\frac{U}{Q} \right). \quad (3)$$

The error on θ is given by $\sigma_\theta = \frac{\sigma_p}{p} \times 28^\circ 6$.

The polarization data were binned to a resolution of 18 arcsec to improve the SNR. Vectors were chosen for the catalogue if $\sigma_p < 4$ per cent, thereby removing unreliable vectors in regions of high noise. We have also imposed a cut of $\text{SNR} \geq 2$ in p as vectors with below this level have large errors in θ and the bias correction we make is really only applicable at $\text{SNR} \geq 2$ (Hildebrand et al. 2000). The SNR cut affects only 2/57 vectors and has no consequences for our results (see Section 3.2). The absolute accuracy in position angle is limited by the systematics of removing the sky noise. This was found to be $\pm 6^\circ$.

As discussed by Greaves et al. (2003), there is a minimum believable polarization percentage within the main beam of SCUBA polarization maps due to potential contamination of the polarization signal from the extended sidelobes of the JCMT beam. The value of the minimum believable polarization is given by the relation

$$p_{\text{crit}} \geq 2p_{\text{sl}} P_{\text{sl}} \frac{S_{\text{sl}}}{S_{\text{mb}}}, \quad (4)$$

where p_{sl} is the polarization in the sidelobe (i.e. off-centre position) and P_{sl} is the power in the sidelobe relative to the main beam (measured from planetary observations). The flux at the position of an off-centre source relative to the flux at the map centre is given by $S_{\text{sl}}/S_{\text{mb}}$. We have used observations of Uranus, obtained at the time of the Cas A observations, to assess the value of p_{crit} and thereby measure the sidelobe polarization for our science data.

The highest value of p_{crit} will be measured for the largest ratio of $S_{\text{sl}}/S_{\text{mb}}$. This value arises for our observations of the northern rim of Cas A, in which the brightest peak in the field of view does not lie at the array centre. For these observations, we measure a flux ratio of 1.1 relative to the centre of the array. The power in

Table 1. Summary of VLA observations.

Configuration	Date	Bandwidth	Duration
A	2000.9	6.25 MHz	12 h
B	2001.2, 2001.3	12.5 MHz	11 h
C	2000.3	25.0 MHz	6.0 h
D	2000.7	25.0 MHz	4.5 h

the beam within this annulus ($49.0 < \sqrt{\Delta\alpha^2 + \Delta\delta^2} < 61.8$ arcsec, where α and δ represent RA and Dec.) is 0.014 relative to the main beam, and the IP measured within the same annulus is 9.2 ± 4.6 per cent. The highest value of p_{crit} is therefore 0.3 ± 0.2 per cent. We can therefore accept that all values of p in excess of 0.5 per cent arise from the remnant itself. Since all measured values exceed this threshold by a significant margin, it is clear that none of the measurements are due to polarization in the sidelobe positions.

2.2 Radio observations

Cas A was observed with the National Radio Astronomy Observatory's (NRAO)² Very Large Array (VLA) in 2000–01 using all four configurations from the most extended (A) to the most compact (D). Data were taken at four frequencies, 4605, 4720, 4860 and 4995 MHz, as summarized in Table 1.

Standard calibration procedures were employed, as outlined in the AIPS cookbook³ using 3C 48 to set the flux density scale, 3C 138 to calibrate the polarization and J2355+498 as a local phase calibrator. After initial calibration, multiple passes of self-calibration were performed to improve the antenna phase solutions.

The AIPS maximum entropy deconvolution routine `vTESS`, which maximizes smoothness in an image, was used to restore the total intensity images and the corresponding routine `uTESS`, which maximizes emptiness in an image, was used to restore the Stokes Q and U images. An 18-arcsec beam (FWHM) was used for deconvolution, to match the resolution of the submm data. The standard primary beam attenuation correction was applied in the `vTESS` and `uTESS` routines. The total restored flux density was 788 Jy. Noise-corrected, linearly polarized intensity, polarization percentage and polarization PA images were made from the Stokes I , Q and U maps. The total polarized flux density was 28.9 Jy, resulting in an average polarization percentage of 3.7 per cent.

To enable a comparison with the submm data, the radio IQU datacube was aligned with the submm pixels using the Kernel Application Package (`KAPPA`) task `WCSALIGN`. Polarization vectors were then calculated in the same way as for the submm data, but using bespoke `MATLAB` scripts. Radio vectors with $\sigma_p < 2.4$ were chosen, providing complete coverage of the regions where we have submm vector information.

3 RESULTS

The SCUBA 850- μm polarimetry vectors are shown in Fig. 2, alongside the 5-GHz radio vectors. The underlying images are the 850- μm scan-map from D03 and the 5-GHz image, both convolved to the

² NRAO is a facility of the National Science Foundation operated under cooperative agreement by Associated Universities, Inc.

³ www.aips.nrao.edu/cook.html

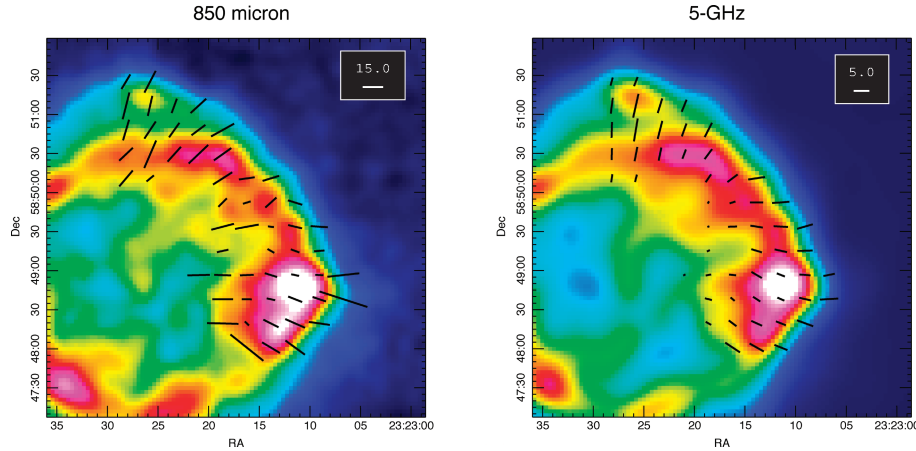


Figure 2. Left-hand side: 850- μm polarimetry vectors overlaid on the 850- μm map from D03. Right-hand side: 5-GHz polarimetry vectors overlaid on the 5-GHz map. All maps are at the same resolution, 18 arcsec. Vectors are rotated by 90° to show the direction of the magnetic field. The orientation of the submm vectors clearly traces the approximately radial B field of the remnant. The 5-GHz vectors have been corrected for an average rotation measure of -110 rad m^{-2} .

same resolution as the binned polarimetry data. The length of the vectors represents the degree of polarization, p , and their PA shows the direction of the magnetic (B) field (i.e. the E vectors measured from the Stokes parameters have been rotated by 90° for display purposes).

These images clearly show that the submm emission is significantly more polarized than the radio emission, with vectors that trace the approximately radial magnetic field in the remnant. Both traits indicate a source of polarized emission in Cas A above a general extrapolation of the synchrotron polarized flux density.

We will now investigate in more detail the robustness of this result and explore whether the submm polarization is due to dust or synchrotron emission.

3.1 Robustness of results

In this section, we will describe our investigation into the robustness of the data through comparing several reductions of the polarimetry data and also through a simulation of the effects of chopping. We conclude that the data are robust and that chopping cannot conspire to affect our conclusions. Readers who wish to skip the technical details can move on to Section 3.2.

3.1.1 Data-reduction issues

We explored the effect of using different sky bolometers and clipping thresholds whilst reducing the submm data (Section 2). The choice of sky bolometers is important as several effects can cause a bolometer’s signal to vary with time during a polarimetry observation.

(i) A changing sky level, which should correlate across all bolometers.

(ii) Bolometers jiggling on and off a bright source. This is the rationale behind choosing off-source bolometers to remove sky variations across the whole array.

(iii) Bolometers may lie on regions of the same brightness throughout an observation but see polarized emission which changes as a function of wave-plate angle, and therefore as a function of time within the observation.

If bolometers displaying effects (ii) or (iii) are used to remove sky noise, they could introduce a temporal signal variation to the rest of the array and cause systematic changes in the derived polarization properties.

We tried two sky-removal techniques: the first used as many bolometers as possible, whilst avoiding bright emission regions; a second, more conservative approach used only bolometers two rows away from bright emission. We found small changes in p ($\Delta p = -0.3$) and θ ($\Delta\theta = -7^\circ$), but the differences between the reductions are consistent with the errors derived from the distributions in each map ($\sigma_p = 1.2$, $\sigma_\theta = 4^\circ$). As the first method uses bolometers which may have jiggled on to polarized emission, we will use the second, more conservative approach for the rest of the analysis. Our overall conclusions are unaffected by this choice of sky-removal technique.

We have also compared our maps to the data presented by Matthews et al. (2008) where the mean sky level was not removed from the array (only the variations are removed) and bolometers showing excess noise were flagged aggressively, resulting in the removal of around 30 per cent of the data. We have taken a slightly different approach, flagging only the four bolometers with clear excess noise, plus one that was dead: around 13 per cent of the data in total. The time series of many bolometers removed by Matthews et al. (2008) displayed momentary spikes but were otherwise in line with the rest of the array. We de-spiked these by flagging any data more than 3σ from the mean. Overall, the mean p and θ derived from both reductions are consistent within the errors ($\Delta p = 1.0$ and $\Delta\theta = -5^\circ$). We conclude that the data are robust to minor changes in the data reduction procedure.

3.1.2 Chopping

We investigated the effects of chopping on to either polarized or unpolarized emission, something which can potentially have a serious impact on submm polarimetry data (Hildebrand et al. 2000). We synthesized Q and U for our reference positions using either the radio values scaled to 850 μm or assuming a value for p and θ for the interstellar medium (ISM) surrounding Cas A (these are described in more detail below). The Q and U values from our submm polarimetry data were then corrected by adding half of the

Table 2. Results of simulated chopping on to polarized emission.

Model	Submm I map	p_{cor}	W: western field			N: northern field			
			p_{chop}	Δp	$\Delta\theta$	p_{cor}	p_{chop}	Δp	$\Delta\theta$
Scaled radio $Q, U \times 3$	A	11.1	11.9	+0.8	+0.4	13.0	13.7	+0.7	+0.9
	B	8.2	8.7	+0.4	+0.4	11.1	12.2	+1.0	+0.9
	C	10.6	11.1	+0.5	+0.4	See note*			
<i>Archeops</i> 1 $p = 23$ per cent, $\theta = -\pi/3$	A	10.7	11.9	+1.2	+1.2	12.5	13.7	+1.2	-0.7
	B	8.2	8.7	+0.5	+0.9	10.3	12.2	+1.9	-2.7
	C	10.4	11.1	+0.7	+0.5				
<i>Archeops</i> 2 $p = 12$ per cent, $\theta = \pi/8$	A	11.6	11.9	+0.3	-0.3	13.5	13.7	+0.2	+0.5
	B	8.5	8.7	+0.2	-0.3	11.7	12.2	+0.5	+1.6
	C	10.9	11.1	+0.2	-0.1				
Observed map	Polarimetry		12.6 \pm 1.2				15.1 \pm 0.8		

Notes: Column (1) refers to the model used for Q and U in the reference positions; Column (2) submm scan-map used to determine the reference I value and combined with the measured submm Q and U to produce the quoted p values (see text); Column (3) mean p in the corrected map; Column (4) mean p in the ‘chopped’ map, error on the mean p is similar to that quoted for the polarimetry in the final row of the table (~ 1 per cent in each field); Column (5) $\Delta p = p_{\text{chop}} - p_{\text{cor}}$; Column (6) $\Delta\theta = \theta_{\text{chop}} - \theta_{\text{cor}}$. Columns (3)–(6) are repeated for positions W and N which each have different reference chop positions. *Scan-map C cannot be used for position N as the background is too negative.

Q and U values found at each reference position. The I values were taken from the 850- μm scan-maps, which comprised the D03 flattened and unflattened reductions (hereafter A and B), the former with large-scale undulations removed, and the map used by Krause et al. (2004) (hereafter C). We created a simulated ‘chopped’ image from our measured Q and U values, and a ‘chopped’ I image from the scan-map after processing it with the chopping simulator. This is intended to represent the data we measure. We then correct for the chopping in Q , U and I and produce a ‘corrected’ map. This assumes, of course, that the scan-maps provide a good representation of unchopped data (they are the best we have). Chopping on to unpolarized flux should not affect θ but will influence p . We have thereby simulated the range of plausible structures around Cas A to probe the possible systematics. In utilizing the unflattened scan-maps, we have assumed that any structure is real and not an artefact of the data reduction.

In the first instance, we assumed that only flux associated with the remnant was polarized and used the radio Q and U maps to estimate the flux of polarized synchrotron in the reference beams. We accounted for a rotation of 24° in going from 5 GHz to 850 μm , in line with the rotation measures derived by Jones et al. (2003) and Anderson, Keohane & Rudnick (1995). We scaled the radio Q and U values to 850- μm using the value of the synchrotron spectral index at the reference points ($\alpha \sim -0.74$) and increased the polarized flux in the reference positions by a factor of 3, roughly the average ratio of $p_{\text{submm}}/p_{\text{radio}}$ that we observe, to allow for the reference beams being polarized at the same level as the central field. The results are summarized in Table 2. We found that chopping on to remnant emission polarized at the level seen in the submm would have a small effect on the submm vectors, with an average increase in p of +0.6 per cent and an average rotation of +0.4.

We next investigated the possibility that any foreground submm emission in the reference positions is polarized. We allow all of the submm emission in the reference positions to be polarized at the level found in clouds in the vicinity of Cas A by the *Archeops* submm balloon experiment (Benoît et al. 2004), which is 23 per cent at $\theta = -\pi/3$ and 12 per cent at $\theta = \pi/8$. It is not certain that the Cas A foreground emission is polarized at this high level as the clouds in Benoît et al. are $>2^\circ$ away, but we consider this as the most conservative case. We find that the difference in the chopped and unchopped maps is $\Delta p = 0.3$ – 1.2 in field W and $\Delta p = 0.2$ – 1.9

in field N. The rotation introduced by chopping is small, the largest being +1.2 in W and -2.7 in N. These simulations are shown in Fig. 3 and the results summarized in Table 2. None of the small changes introduced by chopping alters our conclusions.

3.2 Submm and radio polarization properties

Polarization vectors were created as described in Section 2.1 using the same positions in the observed 850- μm and 5-GHz images. We also predict the observed polarization expected at 850 μm , given the measurements in hand at 5 GHz and assuming that the excess submm emission is unpolarized. We scale the 5-GHz Q and U fluxes using a 1.4/5 GHz spectral index map. We use the submm scan-map from D03 as the I image, since this exceeds the predicted synchrotron flux by ~ 30 per cent (due to dust emission, either in the SN remnant or in front of it). We then calculate p using the scaled radio Q and U data and the submm I data. This is the polarization we would expect if the submm I emission consisted of synchrotron and unpolarized dust.

A comparison of the p distributions in the radio and submm wavebands is shown in Fig. 4, where it is clear that the submm emission shows a significantly higher degree of polarization than does the radio. The means of the distributions are $p_{\text{submm}} = 13.5 \pm 0.8$ per cent and $p_{\text{radio}} = 3.7 \pm 0.2$ per cent when selecting vectors at $p/dp \geq 2$ and $dp < 4$ per cent in the submm waveband. If the SNR threshold is ignored, the mean p_{submm} drops slightly to 12.9 ± 0.9 per cent. The means are thus different at the $>8\sigma$ level. If we compare to the predicted values at 850 μm (dashed histogram in Fig. 4) the difference becomes even more pronounced. The results of the chopping simulations suggest a minor reduction in p_{submm} of order 0.7 per cent may be required, but there appears to be no possibility of reconciling the two distributions.

Having established a clear excess in polarization at 850 μm , we now wish to understand whether this difference is due to a reduction in the level of synchrotron polarization between 850 μm and 5 GHz via a depolarizing mechanism in the remnant or to an extra source of polarized emission at 850 μm (i.e. aligned dust grains).

Synchrotron emission in SN remnants should be highly polarized (~ 70 per cent), but observed polarizations at radio frequencies in young remnants like Cas A are typically much lower,

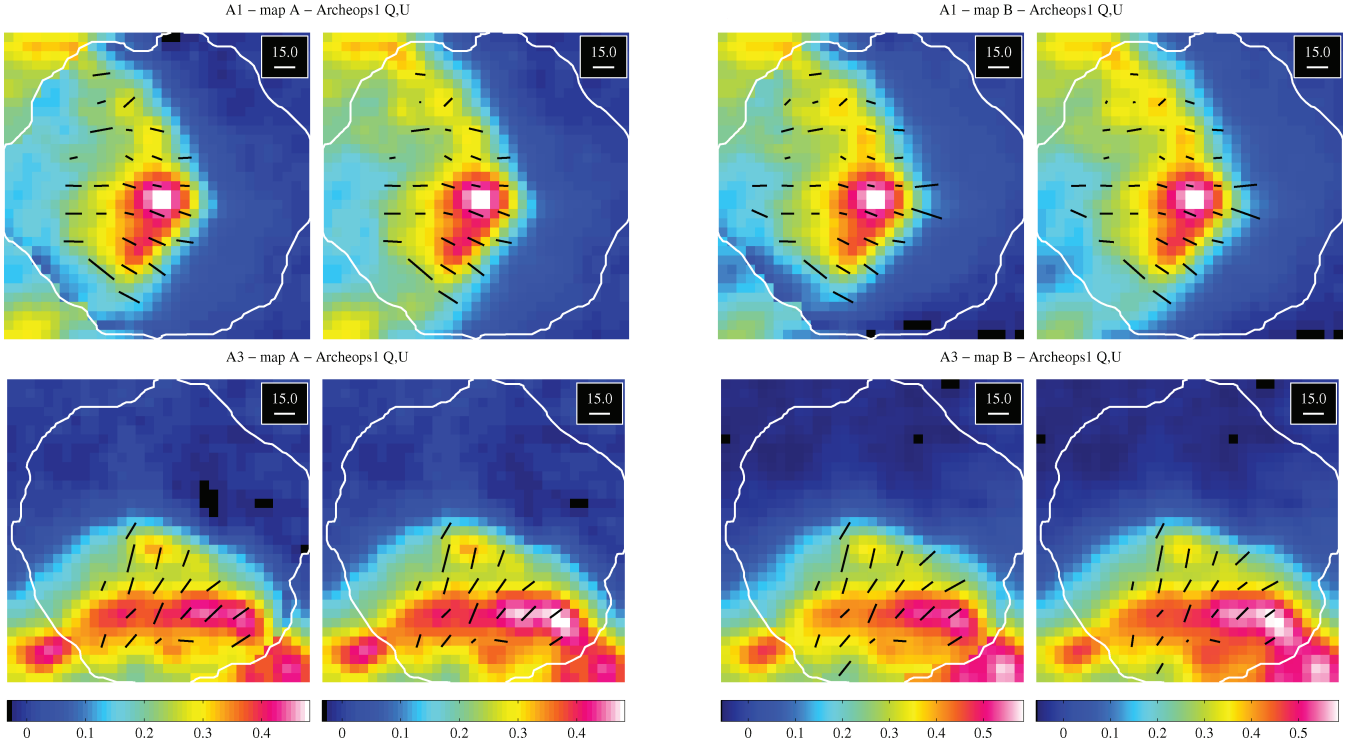


Figure 3. Simulated chopped and unchopped images as described in Section 3.1. On the left-hand side of each subpanel is the ‘chopped’ image, meant to represent the polarimetry data. Next to it on the right-hand side is the corrected image. The upper row is for region W and the lower row is region N. The scan-maps used are A and B and the Q and U model is *Archeops 1* (see Table 2 and Section 3.1 for a detailed description). The effects of chopping on I can be mostly seen at the edges of the fields where the edge of the remnant was chopped on to (see Fig. 1).

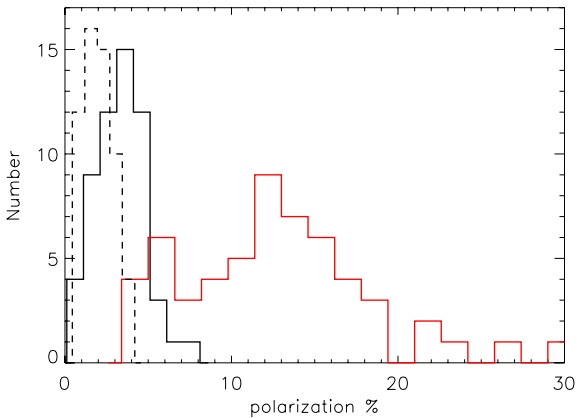


Figure 4. Histogram showing the distribution of p for the 5-GHz data (black) and the 850- μm data (red). The distributions are significantly different. The predicted polarization at 850 μm , using the 5-GHz data as described in the text, is shown by the dashed line.

implying that the magnetic field is highly disordered on scales below 1 arcsec (Milne 1987). Another cause of reduced polarization at radio wavelengths is rotation due to the Faraday effect, in which the plane of polarization is rotated as the polarized waves pass through a magnetized plasma. This effect is wavelength-dependent, with longer wavelengths suffering more rotation. Emission from regions at different depths in the plasma of Cas A will be rotated by differing amounts as they travel to the observer. This causes ‘internal depolarization’ at the wavelengths which undergo the most rotation.

Depolarization at radio frequencies has been studied in Cas A and found to be negligible at frequencies of $\gtrsim 5$ GHz. From 5 GHz to 2.2 μm , the fractional synchrotron polarization remains roughly constant (4–7 per cent; Kenney & Dent 1985; Anderson et al. 1995; Jones et al. 2003) which suggests that the much higher polarizations observed at 850 μm cannot be due to synchrotron radiation. In some specialized geometries, depolarization can lead to an increase in fractional polarization followed by a decrease at successively larger wavelengths, but this occurs only under conditions of very strong depolarization (≥ 10 ; Cioffi & Jones 1980), which does not apply in Cas A above 5 GHz. The lack of depolarization at 5 GHz thus implies that the high 850- μm polarizations arise from an independent source.

Another piece of evidence for internal depolarization could have come from comparisons of depolarization with X-ray brightness, serving as a proxy for the density of the depolarizing thermal electrons. Indeed, Anderson et al. (1995) showed a very strong correlation between the X-ray brightness and the depolarization of emission between 5 and 1.4 GHz, arguing for internal depolarization at the low radio frequencies. However, no such dependence is seen in our comparison of depolarization between 850 μm and 5 GHz and the X-ray brightness (Fig. 5, left-hand side). Thus, the high fractional polarizations at 850 μm must arise from another cause. This 850- μm independence is also demonstrated in the plot of p_{radio} versus p_{submm} in Fig. 5 (right-hand side), where no correlation is seen.

We now turn to the PA of the polarization. In Fig. 6 (left-hand side), we show the PAs (θ) of the radio versus the submm. Filled symbols indicate the western region and open symbols the northern region. There is a very good correlation between PAs contrary to

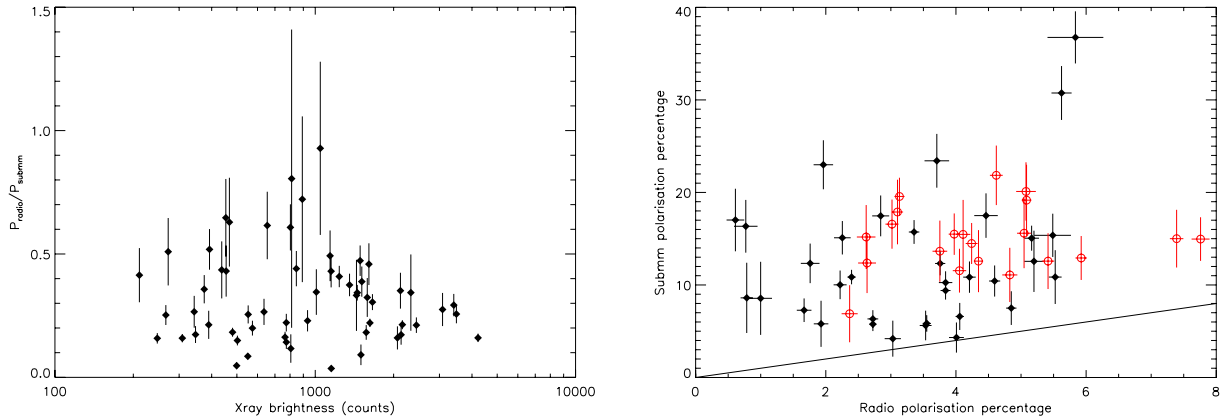


Figure 5. Left-hand side: depolarization from 5 GHz to 850 μm as a function of X-ray brightness. There is no clear relationship, unlike the 1.4-5 GHz depolarization which correlates strongly with X-ray brightness (Anderson et al. 1995). Right-hand side: radio polarization versus submm polarization. The line shows a one-to-one correspondence. Filled black diamonds are the western region while red open circles are the northern region. There is no obvious correlation.

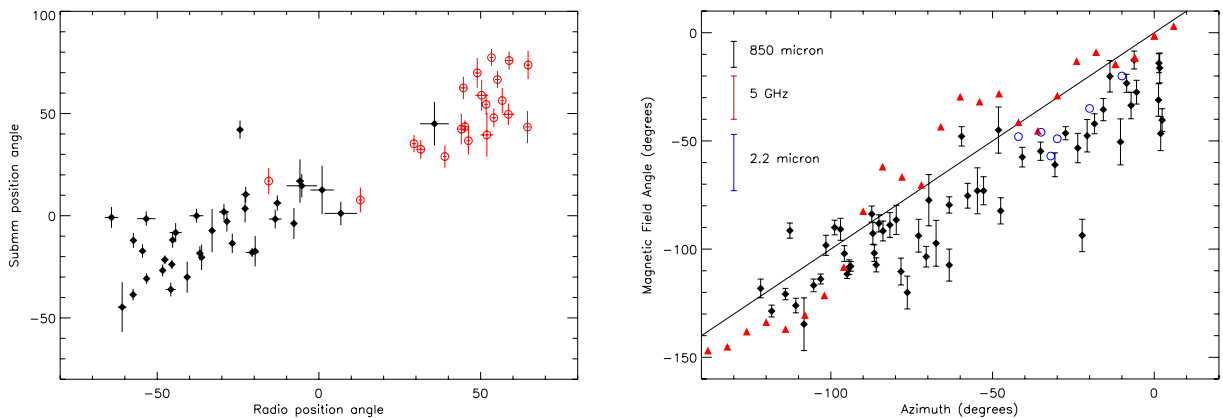


Figure 6. Left-hand side: radio versus submm position angles. Filled symbols represent the western region while open symbols represent the northern region. There is a very good correlation between the direction of the radio and submm polarization vectors. Right-hand side: inferred magnetic field angle ($\text{PA} - 90^\circ$) versus azimuth angle (0° for celestial north). Solid diamonds are 850- μm PAs; red triangles are 5-GHz PAs from Anderson et al. (1995) corrected for the local RM as described in the text; blue open circles are 2.2- μm PAs from Jones et al. (2003). Systematic errors bars are shown in the top left. The solid line shows a pure radial alignment.

the lack of correlation between polarization strengths. This suggests that the submm polarization is largely arising from a different physical mechanism than the synchrotron radio polarization. However, both polarization signals reflect the same underlying magnetic field in Cas A. This is further demonstrated in Fig. 6 (right-hand side), where we show the PAs of the radio and submm and 2.2- μm polarization vectors (Jones et al. 2003) as a function of azimuth. The radio measurements have been corrected for the local Faraday rotation, redetermined from the data of Anderson et al. (1995). They quoted an average value for the rotation measure (RM) of -110 rad m^{-2} , while we determine a range of values from -50 to -302 rad m^{-2} for our range of azimuths. The extrapolated rotations at 850 μm are <0.01 , so no correction for Faraday rotation has been made for those or for the 2.2- μm data.

There is a very good correlation between all three sets of measurements, suggesting that whatever is responsible for the extra polarization signal in the submm waveband is related to the same magnetic fields that are responsible for the synchrotron emission at 5 GHz and 2.2 μm and, perforce, is intrinsic to Cas A and is not due to foreground material. The small mean offset between the cor-

rected 5-GHz PAs and those at 850 and 2.2 μm are consistent with the systematic uncertainty in the RM correction. To first order the PAs all provide strong evidence for a radial magnetic field, as is common in young SN remnants (Anderson et al. 1995).

If we take the submm and 2.2- μm magnetic field PAs at their face value, ignoring the systematic uncertainties, they agree very well with each other and are systematically offset from a radial angle by $\sim 10^\circ - 20^\circ$ in a clockwise direction. At present, there is no apparent reason for this offset.

4 DISCUSSION

Since we cannot explain the submm polarization as arising from synchrotron emission we will now consider the most likely alternative – that it is due to dust aligned with the magnetic field in the remnant. We will estimate p_d , the polarization fraction of the dust in the remnant. We know that the submm flux we measure is a combination of radio synchrotron and thermal emission from dust, such that $I_s = I_r + I_d$. Similarly, we can write that $Q_s = Q_r + Q_d$ and $U_s = U_r + U_d$. We can also express Q and U in terms of I , p

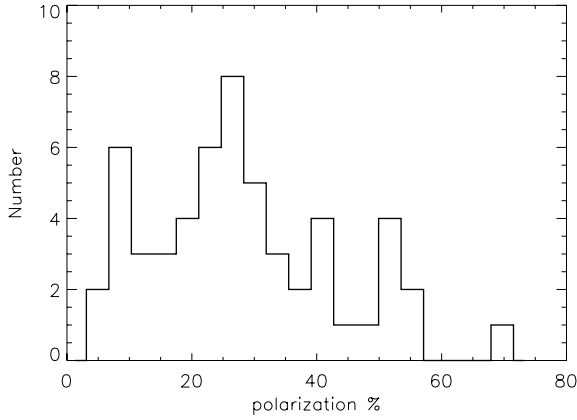


Figure 7. Histogram of dust polarization fraction, p_d , calculated using equation (6).

and θ , as $Q = Ip \cos(2\theta)$ and $U = Ip \sin(2\theta)$. Combining these equations and solving for dust polarization, p_d , gives

$$p_d = \frac{[(I_s p_s - I_r p_r)^2 + 2 I_s p_s I_r p_r (1 - \cos 2(\theta_s - \theta_r))]^{1/2}}{I_d}, \quad (5)$$

which for $\theta_s = \theta_r$ simplifies to

$$p_d = (p_s - p_r) \frac{I_r}{I_d} + p_s. \quad (6)$$

The fractional dust polarization calculated using equation (6) is unprecedented, with an average $p_d = 30 \pm 2$ per cent. A histogram of p_d is shown in Fig. 7. Equation (6) assumes that the polarized synchrotron and dust radiation is emitted with the same intrinsic PA (i.e. aligns with the B field in the same way) and that any rotation between 5-GHz and 850- μm vectors is due to Faraday rotation at 5 GHz. This is a reasonable assumption given Fig. 6. We obtain a slightly higher value for p_d (33 per cent) if we use the difference between the RM corrected 5-GHz PA and the submm PA in equation (5) instead.

We can create a map of 850- μm dust flux density, I_d , by scaling the 5-GHz map to 850 μm as described in Section 3.2. Subtracting the scaled synchrotron map from the 850- μm image leaves the 850- μm emission due to dust. This dust map⁴ is shown in Fig. 8, with the dust polarization calculated from equation (6). Over-plotted are CO(2–1) contours from Eales et al. (in preparation). This shows three things: first, there is dust emission in the northern part of the remnant, but no corresponding CO emission; secondly, the level of submm polarization anticorrelates with the CO contours; the dust polarization being lowest at the western peak, consistent with the suggestion by Krause et al. (2004) and Wilson & Batrla (2005) that its submm emission is contaminated by foreground clouds; thirdly, there is polarized dust emission in both the north and the west.

The polarization signal is correlated with the magnetic field in the remnant, which means that some of the emission in the western region must be associated with the remnant. None of the dust intensity or polarized flux in the north is associated with molecular material. Thus, the finding of Krause et al. (2004) that there is ‘no cold dust in Cas A’ is demonstrably incorrect. The average dust polarization around the western peak is 13.7 ± 1.4 per cent; in the north, away

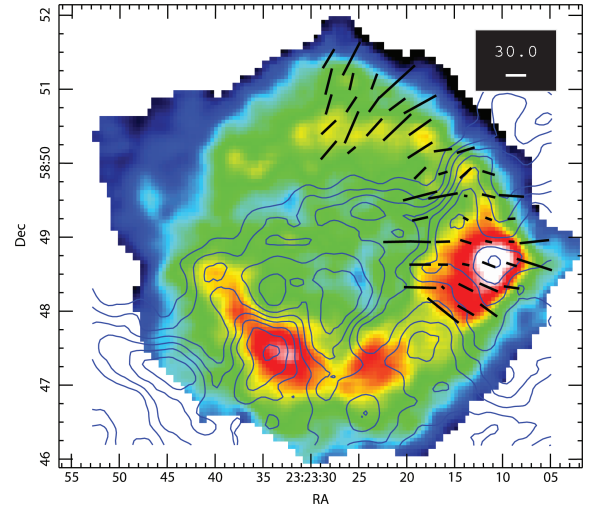


Figure 8. Synchrotron-subtracted 850- μm image, showing the location of the dust. Overlaid are the dust polarization vectors calculated using equation (6). Also shown in blue are CO(2–1) contours, at the same resolution (Eales et al., in preparation). CO contours coincide with the western dust peak, but the dust polarization at these positions indicates that some of the 850- μm emission must be due to dust in the remnant. The decrease in dust polarization at the CO peak in the west is consistent with some fraction of the submm emission at this location being due to foreground material, associated with the CO. Note that there is no CO emission coincident with the dust emission in the north.

from the CO, it is 39.4 ± 3.2 per cent. If we assume that the intrinsic value of p_d is similar throughout the remnant, we can use the uncontaminated values in the north to estimate the contribution of the foreground material to the western peak. Since $p \propto 1/I$, we simply correct the dust flux in the western peak by the ratio $13.7/39.4 = 0.34$, which gives a flux density of ~ 0.8 Jy intrinsic to Cas A at the western peak. In order to make a comprehensive correction for the intervening foreground material, a full set of molecular gas tracers must be observed over the whole remnant. This data set does not yet exist and therefore we cannot make a definitive measurement of the total submm flux associated with the remnant at this time. We can, however, estimate a conservative lower limit by assuming that only the polarized flux density at 850 μm (~ 30 per cent) is intrinsic to the remnant. The integrated flux density from the dust map in Fig. 8 is $S_{850} = 20.1$ Jy,⁵ and taking the average 30 per cent polarized fraction as the minimum gives us a total lower limit on the dust flux for Cas A at 850 μm of 6.0 Jy, based on our submm polarimetry.

To convert this flux density into a dust mass, we must assume a value for the dust mass absorption coefficient κ_{850} . In our previous work (D03), we used a value which was derived from laboratory studies of cosmic dust analogues which were amorphous, non-spherical or aggregates. This gave a high value of $\kappa_{850} = 0.76 \text{ m}^2 \text{ kg}^{-1}$. If we apply this value to our flux measurement and use a temperature of $T_d = 20$ K (which comes from fitting the SED from the IR submm), we get a dust mass estimate for Cas A of $\sim 1.0 M_\odot$. This value is consistent with theoretical predictions for SN dust yields (e.g. Todini & Ferrara 2001; Nozawa et al. 2003; Bianchi & Schneider 2007) and sufficient to explain the dust at

⁴ This map differs slightly from that in D03 as we have used a more accurate, spatially varying spectral index to extrapolate the radio synchrotron flux to the submm waveband.

⁵ This is higher than the value of 15.9 Jy quoted in D03 due to the lower synchrotron contribution at 850 μm when using a varying radio spectral index.

high redshift (Morgan & Edmunds 2003; Dwek et al. 2007). This is also an upper limit to the possible mass of dust in Cas A given the masses of condensable elements formed in SNe with progenitor masses in the range applicable to Cas A (13–20 M_{\odot} – as suggested by the recent determination of the type of Cas A as a IIb by Krause et al. (2008)). According to nucleosynthetic models by Limongi & Chieffi (2003), SNe with progenitors in this mass range could produce 0.5–1.0 M_{\odot} of dust if the condensation efficiency were 100 per cent.

We can also look at new values for κ_{850} which have been derived from models of dust formation in SNe similar to Cas A. Values range from $\kappa_{850} = 0.2 \text{ m}^2 \text{ kg}^{-1}$ from Bianchi & Schneider (2007) to $\kappa_{850} = 0.049 \text{ m}^2 \text{ kg}^{-1}$ for a Cas A-like case from Nozawa et al. (2003) and Kozasa et al. (2008). These κ values produce dust masses in the range 3.8–15 M_{\odot} . Given the above discussion on the available mass of condensable elements, these values are not physically plausible. This suggests that the dust which is emitting the polarized radiation at submm wavelengths is not currently predicted by the dust formation models and is not necessarily the same as the dust which is emitting at the shorter FIR wavelengths seen by *Spitzer* and *IRAS*. The SNe formation models currently only deal with spherical grains, but in order to produce polarized emission the grains must be elongated to some degree. Further development of the dust formation models may be required in order to produce grains which can reproduce the quantity and polarized nature of the submm emission in Cas A. In order to have a physically plausible mass of dust the emissivity of the dust must be high – at least as high as that found in the laboratory studies of amorphous and aggregate grains.

The highly elongated iron needle grains proposed by Dwek alleviate the emissivity issue, as for long enough axial ratios they have emissivities many orders of magnitude higher than spheroidal non-conducting grains. Graphite whiskers may also provide a similar solution, especially in light of their recent discovery in meteorites (Fries & Steele 2008). Iron or graphite needles could reduce the dust mass required although a full analysis of the properties of such grains which match the new observations is beyond the scope of this paper. We therefore do not rule out such exotic grains and will consider them in more detail in a future paper (Gomez et al., in preparation).

4.1 Grain alignment

What does this polarization fraction tell us about the properties of the dust in Cas A? Average polarization fractions in typical interstellar and molecular clouds are of the order 2–7 per cent (Hildebrand et al. 2000; Matthews & Wilson 2002; Curran & Chrysostomou 2007) though some clouds have values as high as 15–20 per cent (Benoît et al. 2004). We are unaware of any measurements as high as those quoted here, which suggests that either the dust or the alignment mechanisms in Cas A differ – perhaps unsurprisingly – from those in the general ISM.

Observations of polarized starlight and thermal emission from dust mean that there must be a population of dust grains which are non-spheroidal and a mechanism capable of aligning the grains so that an appreciable polarization signal can be detected. The details of how interstellar dust aligns so efficiently, despite impacts by gas atoms acting to randomize their orientations, have kept theorists busy for half a century. The original proposal by Davis & Greenstein (1950, 1951) suggested paramagnetic alignment, where the axis of rotation of the slightly elongated grains becomes aligned with the B field through magnetic dissipation. This theory was unable to explain the polarization levels observed in the ISM and star-

forming regions because the time-scales for alignment are longer than the time-scales for randomization by collisions with the gas.

There have been many significant improvements to the theory of grain alignment in recent years – see Lazarian (2007) for an excellent review. Several mechanisms are now thought to operate in different astrophysical environments. Briefly, these comprise radiative torques (Dolginov 1972; Draine & Weingartner 1996; Lazarian & Hoang 2007a; Hoang & Lazarian 2008a), mechanical alignment in a supersonic or subsonic gas flow (Gold 1952; Roberge, Hanany & Messinger 1995; Lazarian 1997; Yan & Lazarian 2003; Lazarian & Hoang 2007b) and superparamagnetic alignment (Lazarian & Hoang 2008).

The strong and turbulent magnetic field in Cas A ($B \sim 0.5 \text{ mG}$; Wright et al. 1999), together with the large abundances of heavy elements and the presence of a hot X-ray plasma, means that certain mechanisms may be particularly applicable to the environment of Cas A. Pinwheel torques arising from the interaction of grains and electrons in a hot plasma (Hoang & Lazarian 2008b), supersonic mechanical alignment, subsonic mechanical alignment through magnetohydrodynamic turbulence (Yan & Lazarian 2003) or grains with superparamagnetic (e.g. Fe) inclusions (Lazarian & Hoang 2008) can all lead to highly efficient alignment. The time-scales they have to operate is small in astrophysical terms, as the explosion of Cas A occurred only ~ 300 yr ago. We note that the low synchrotron polarized fraction indicates a turbulent and disordered magnetic field on sub-arcsecond angular scales. This acts to reduce the observed polarization as random orientations are averaged within the synthesized beam. If the dust grains were aligned with this tangled small-scale magnetic field then we might expect a similar beam depolarization effect to operate at submm wavelengths. However, this would give rise to unphysical intrinsic dust polarization fractions and so we believe that the alignment mechanism must be operating on larger scales. The radial B field in Cas A is ordered on large scales and thought to arise from Raleigh–Taylor instabilities at the reverse shock boundary (Gull 1975). These large-scale radial motions may also be responsible for aligning the dust in Cas A.

Even if full alignment is theoretically possible, the line-of-sight angle to the B field in Cas A together with the random alignment of orientations along the line of sight and within the beam should all act to reduce the measured polarization. That we still observe such a high f_{pol} indicates that the grains themselves are emitting strongly polarized radiation. For ideal alignment and line-of-sight viewing conditions $f_{\text{pol}} \sim 30$ per cent can be achieved with only moderately non-spherical grains of astronomical silicate, with axial ratios of between 1.4 and 1.7 for oblate and prolate grains, respectively (Padoan et al. 2001). Thus, the level of polarization *per se* is not, on its own, strong evidence for needle like grains. An estimate of the aligned fraction would be required in order to constrain the shape of the grains.

A full application of the various grain alignment models to Cas A is beyond the scope of this paper but these data should provide an interesting test of alignment theories and in time should also shed light on the nature of the grains responsible for the polarized submm emission.

5 SUMMARY

(i) We have discovered unprecedented levels of submm polarization towards the Cas A SN remnant, significantly in excess of that expected from the radio synchrotron, and correlated with the magnetic field direction in Cas A.

(ii) There is no currently known way to produce the polarized submm emission from a synchrotron process; a depolarizing mechanism capable of producing a peak in f_{pol} as a function of wavelength would be required.

(iii) The polarized emission is therefore strong evidence that a significant fraction of the cold dust detected by D03 is associated with the SN remnant. Further strong evidence is that there is both polarized and unpolarized dust emission in the northern region, which is not affected by foreground molecular clouds.

(iv) A high dust emissivity is required in order to stay within the constraints of the mass of condensible elements available to form dust. This limit on the emissivity is not consistent with that currently predicted for dust formed in SNe.

(v) The strength of the polarization signal is unprecedented in the general ISM and indicates a highly efficient alignment mechanism at work in Cas A. These data provide a stringent test of grain alignment mechanisms, given the very short time-scale available, ~ 300 yr.

(vi) Alternatively, the strong signal may arise in exotic grains such as iron or graphite needles. Such grains would naturally produce a higher emissivity and keep within the mass budget.

(vii) Higher-resolution polarimetry at $850 \mu\text{m}$ is required to confirm the polarization signal and provides a comparison at the spatial resolution of the radio synchrotron emission. Measurements of the high-frequency (100–200 GHz) synchrotron polarization are required to test whether a perverse radio depolarization mechanism is at work.

(viii) Future far-IR and submm polarimeters, such as those planned for SCUBA-2 (Bastien et al. 2005) and *FIRI* (Helmich & Ivison 2008), will be able to image the submm polarization in Cas A at higher resolutions and frequencies.

ACKNOWLEDGMENTS

We wish to thank the JCMT staff who were involved in commissioning and maintaining the SCUBA Polarimeter. The data presented here were awarded under programme M04AU10. We also thank A. Chrysostomou, R. Curran, J. Greaves and G. Scheiven for helpful discussions on polarimetry data reduction, T. J. Jones for comments on the 2.2- μm data, S. Bianchi and T. Nozawa for discussions related to the emissivity, A. Lazarian and B. Draine for very helpful comments on grain alignment and polarization.

REFERENCES

Anderson M. C., Keohane J. W., Rudnick L., 1995, *ApJ*, 441, 300
 Bastien P. et al., 2005, *J. R. Astron. Soc. Canada*, 99, 133
 Benoît A. et al., 2004, *A&A*, 424, 571
 Berry D. S., Gledhill T. M., 2001, *Starlink User Note* 223
 Bianchi S., Schneider R., 2007, *MNRAS*, 378, 973
 Blair W. P. et al., 2007, *ApJ*, 662, 998
 Borkowski K. J. et al., 2006, *ApJ*, 642, L141
 Bowden M. et al., 2004, *MNRAS*, 349, 321
 Cioffi D. F., Jones T. W., 1980, *AJ*, 85, 368
 Curran R. L., Chrysostomou A., 2007, *MNRAS*, 382, 699
 Davis L. J., Greenstein J. L., 1950, *AJ*, 55, 71
 Davis L. J., Greenstein J. L., 1951, *ApJ*, 114, 206
 Dolginov A. Z., 1972, *Ap&SS*, 18, 337
 Douvion T., Lagage P. O., Cesarsky C. J., Dwek E., 2001, *A&A*, 373, 281

Draine B. T., Weingartner J. C., 1996, *ApJ*, 470, 551
 Dunne L., Eales S., Ivison R., Morgan H., Edmunds M., 2003, *Nat*, 424, 285 (D03)
 Dwek E., 2004, *ApJ*, 607, 848
 Dwek E., Hauser M. G., Dinerstein H. L., Gillett F. C., Rice W. L., 1987, *ApJ*, 315, 571
 Dwek E., Galliano F., Jones A. P., 2007, *ApJ*, 662, 927
 Fries M., Steele A., 2008, *Sci*, 320, 91
 Gold T., 1952, *Nat*, 169, 322
 Greaves J. S. et al., 2003, *MNRAS*, 340, 353
 Gull S. F., 1975, *MNRAS*, 171, 263
 Helmich F. P., Ivison R. J., 2008, *Exp. Astron.*, 15 (arXiv:0707.1822)
 Hildebrand R. H., Davidson J. A., Dotson J. L., Dowell C. D., Novak G., Vaillancourt J. E., 2000, *PASP*, 112, 1215
 Hoang T., Lazarian A., 2008a, *MNRAS*, 388, 117
 Hoang T., Lazarian A., 2008b, preprint (arXiv:0801.0266)
 Holland W. S. et al., 1999, *MNRAS*, 303, 659
 Jenness T., Lightfoot J. F., 1998, in Albrecht R., Hook R. N., Bushouse H. A., eds, *ASP Conf. Ser. Vol. 145, Astronomical Data Analysis Software and Systems VII*. Astron. Soc. Pac., San Francisco, p. 216
 Jones T. J., Rudnick L., DeLaney T., Bowden J., 2003, *ApJ*, 587, 227
 Kenney J. D., Dent W. A., 1985, *ApJ*, 298, 644
 Kozasa T. et al., 2008, in Henning Th., Gruen E., Steinacker J., eds, *Cosmic Dust – Near and Far*. ASP, Heidelberg, in press
 Krause O. et al., 2004, *Nat*, 432, 596
 Krause O. et al., 2008, *Sci*, 320, 1195
 Lagage P. O. et al., 1996, *A&A*, 315, L273
 Lazarian A., 1997, *ApJ*, 483, 296
 Lazarian A., 2007, *J. Quant. Spectrosc. Radiat. Transfer*, 106, 225
 Lazarian A., Hoang T., 2007a, *MNRAS*, 378, 910
 Lazarian A., Hoang T., 2007b, *ApJ*, 669, L77
 Lazarian A., Hoang T., 2008, *ApJ*, 676, L25
 Limongi M., Chieffi A., 2003, *ApJ*, 592, 404
 Matthews B. C., Wilson C. D., 2002, *ApJ*, 571, 356
 Matthews B. C., McPhee C., Fissel L., Curran R., 2008, *ApJ*, submitted
 Matthews B. C., Wilson C. D., Fiege J. D., 2001, *ApJ*, 562, 400
 Meikle W. P. S. et al., 2007, *ApJ*, 665, 608
 Milne D. K., 1987, *Aust. J. Phys.*, 40, 771
 Morgan H. L., Edmunds M. G., 2003, *MNRAS*, 343, 427
 Murray A. G., Nartallo R., Haynes C. V., Gannaway F., Ade P. A. R., 1997, in Wilson A., ed., *ESA Spec. Pub. Vol. 401, The Far Infrared and Submillimetre Universe*. ESA, Noordwijk, p. 405
 Nozawa T., Kozasa T., Umeda H., Maeda K., Nomoto K., 2003, *ApJ*, 598, 785
 Padoan P., Goodman A., Draine B. T., Juvela M., Nordlund Å., Rögnvaldsson Ö. E., 2001, *ApJ*, 559, 1005
 Priddey R. S., Isaak K. G., McMahon R. G., Robson E. I., Pearson C. P., 2003, *MNRAS*, 344, L74
 Priddey R. S., Ivison R. J., Isaak K. G., 2008, *MNRAS*, 383, 289
 Rho J. et al., 2008, *ApJ*, 673, 271
 Roberge W. G., Hanany S., Messinger D. W., 1995, *ApJ*, 453, 238
 Sparks W. B., Axon D. J., 1999, *PASP*, 111, 1298
 Sugerman B. E. K. et al., 2006, *Sci*, 313, 196
 Todini P., Ferrara A., 2001, *MNRAS*, 325, 726
 Wang R. et al., 2007, *AJ*, 134, 617
 Wang R. et al., 2008, *ApJ*, 687, 848
 Williams R. M., Chu Y.-H., Gruendl R., 2006, *AJ*, 132, 1877
 Wilson T. L., Batrla W., 2005, *A&A*, 430, 561
 Wright M., Dickel J., Koralesky B., Rudnick L., 1999, *ApJ*, 518, 284
 Yan H., Lazarian A., 2003, *ApJ*, 592, L33

This paper has been typeset from a $\text{\TeX}/\text{\LaTeX}$ file prepared by the author.